Available online at www.sciencedirect.com
ScienceDirect
Journal of Power Sources 180 (2008) 309–321
JOURNAL OF POWER SOURCES
www.elsevier.com/locate/jpowsour

Computationally efficient modeling of the dynamic behavior of a portable PEM fuel cell stack

S.P. Philipps, C. Ziegler *

Fraunhofer Institute for Solar Energy Systems ISE, Heidenhofstr. 2, D-79110 Freiburg, Germany

Received 13 April 2007; received in revised form 19 January 2008; accepted 25 January 2008
Available online 16 February 2008

Abstract

A numerically efficient mathematical model of a proton exchange membrane fuel cell (PEMFC) stack is presented. The aim of this model is to study the dynamic response of a PEMFC stack subjected to load changes under the restriction of short computing time. This restriction was imposed in order for the model to be applicable for nonlinear model predictive control (NMPC). The dynamic, non-isothermal model is based on mass and energy balance equations, which are reduced to ordinary differential equations in time. The reduced equations are solved for a single cell and the results are upscaled to describe the fuel cell stack. This approach makes our calculations computationally efficient. We study the feasibility of capturing water balance effects with such a reduced model. Mass balance equations for water vapor and liquid water including the phase change as well as a steady-state membrane model accounting for the electro-osmotic drag and diffusion of water through the membrane are included. Based on this approach the model is successfully used to predict critical operating conditions by monitoring the amount of liquid water in the stack and the stack impedance. The model and the overall calculation method are validated using two different load profiles on realistic time scales of up to 30 min. The simulation results are used to clarify the measured characteristics of the stack temperature and the stack voltage, which has rarely been done on such long time scales. In addition, a discussion of the influence of flooding and dry-out on the stack voltage is included. The modeling approach proves to be computationally efficient: an operating time of 0.5 h is simulated in less than 1 s, while still showing sufficient accuracy.

Keywords: PEM fuel cell; Modeling; Dynamic; Stack; NMPC

1. Introduction

In recent years the interest in using hydrogen fuel cells as power supply for portable electronics has grown substantially. Compared to batteries fuel cell systems can provide a higher energy density and instantaneous refilling while avoiding the problem of self-discharge. However, the use of fuel cells as power supply for electronic products is challenging because the power demand of these applications fluctuates. Due to the limited space in portable electronics the stack can in many cases not be buffered by a battery. Thus, the fuel cell does not usually operate at steady-state. A solid understanding of the dynamic response of a proton exchange membrane fuel cell (PEMFC) under load changes is crucial for reliable and optimized operation [1]. The dynamic behavior of a fuel cell is a highly complex phenomenon, as it involves different length and time scales. The power of a PEMFC also strongly depends on operating conditions such as flow rates, relative humidity and temperature of the gases as well as ambient temperature. Mathematical modeling is a powerful tool for understanding and handling this complexity. Nonlinear model predictive control (NMPC) and online optimization of dynamic processes have attracted increasing attention over the past decade, see e.g. Ref. [2]. In contrast to empirical control strategies based on experimental observations and extensive testing, a model-based control allows faster system development and optimal system operation over a wide range of operating conditions. As a prerequisite, NMPC requires detailed nonlinear process models.

A considerable amount of work has been done thus far to model PEMFCs [3,4]. Most of the models are steady-state, see for example Refs. [5–7]. Less work has been published on dynamic fuel cell modeling. Amphlett et al. [8] modeled the behavior of the stack temperature and the voltage during

* Corresponding author.
E-mail address: christoph.ziegler@ise.fraunhofer.de (C. Ziegler).
URL: http://www.ise.fraunhofer.de (C. Ziegler).

0378-7753/$ – see front matter © 2008 Elsevier B.V. All rights reserved.
doi:10.1016/j.jpowsour.2008.01.089

start-up, shut-down and load-step. In their model only the energy balance of the solid is modeled dynamically whereas all other equations are assumed to be at quasi-steady state for a given solid temperature. Lee et al. [9] used an object-oriented approach based on stationary equations. Dynamic profiles are created by calculating the quasi-stationary solution variables for each time-step. Ceraolo et al. [10] used an isothermal model to simulate the dynamic behavior of the cell voltage to a load change on a time-scale of seconds. Their model was extended to account for non-isothermal conditions by Shan et al. [11]. In recent years several authors have presented dynamic models using a similar approach as Amphlett et al. [8]. Golbert et al. [12] developed a transient along-the-channel model for control purposes, which includes mass balances of liquid water and water vapor. Yu et al. [13] presented another extension of the model of Amphlett, which accounts for the influence of latent heat on the energy balance. Pathapati et al. [14] included dynamic mass balance equations and energy balance equations for the gases. In addition, a term to account for the double layer capacity is presented. The influence of flooding on the dynamic behavior of the stack voltage under isothermal conditions was modeled by McKay et al. [15]. All of these models are reduced in terms of dimensionality and comprehensiveness. In recent years several research groups have published valuable in-depth analyses on the transient behavior of PEM fuel cells using commercial software tools either based on computational fluid dynamics, e.g. Refs. [16–21] or on finite-element, multiphysics simulation approaches, e.g. Refs. [22–25]. These studies help in understanding the fundamental physical processes and interactions within the fuel cell. However, due to the massive computational effort required they are not suitable for online control.

This work presents a dynamic model approach for portable fuel cell stacks. The aim of our work is to model the dynamic behavior of a portable PEM fuel cell stack on relevant time scales for technical applications under the restriction of keeping the computing time short. Therefore, a reasonable compromise between physical accuracy and numerical efficiency is found which makes the model suitable for NMPC. Despite of the number of very valuable contributions to the dynamic fuel cell modeling, a validated model approach, which meets these needs was not found in the literature. Many of the existing models require massive computational effort either in terms of memory usage or computing time or both, e.g. Refs. [16–21,23–25]. Most of the reduced models in the literature are either not designed for NMPC purposes, e.g. Refs. [9,10] or are not validated against experimental data of a PEMFC stack on realistic time scales, e.g. Refs. [11–13]. The reduced model presented here is validated against experimental data of a PEMFC stack for different load profiles on realistic time scales of up to 30 min. The model validation study does also include an analysis of the characteristics of the stack in critical states of operation. The model is non-isothermal and considers the mass transfer and the electrochemical reactions. Moreover, the model accounts for both water vapor and liquid water and for the phase transition. In contrast to previous modeling studies the average liquid water concentration is used to predict flooding of the fuel cell based on the liquid water balance. This can be useful for improved NMPC algorithms. To ease the transfer to different stacks we describe the methods of parameter identification in detail. In order to meet the challenge of realizing sufficiently exact modeling results with short calculation time some strong simplifications are made, which are justified by the good agreement between simulation and experimental results.

2. Model description

2.1. Modeling approach

The PEM fuel cell stack model presented here is dynamic and non-isothermal. The model is based on transient energy and mass balance equations, a membrane model and an electrical model based on the tafel equation. Convective heat and mass transfer within the stack are accounted for dynamically. A mass balance of water in the liquid and vapor phase is included. Condensation and evaporation in the channels as well as water generation at the cathode are accounted for. The membrane model is steady state and accounts for the electro-osmotic drag and back diffusion of water. The steady-state electrical model incorporates the influence of pressure and temperature changes as well as the voltage drop due to activation and ohmic losses.

Fuel cell stacks are commonly characterized by measuring the time evolution of the stack voltage and the stack temperature subject to specific operating conditions like power demand, ambient and gas temperature and gas humidity. In integrated fuel cell systems the stack voltage, the stack temperature and the gas flow rates are usually monitored. The stack model presented here allows the simulation of the most important parameters for the operation of a PEMFC stack. The model considers four monitoring points for the mass and heat balance of the gases: the inlet and outlet of the stack on the anode and cathode side. At these points, gas temperatures and molar fluxes of the different species are considered. The operating conditions at the stack inlets are used as input values of the model. Furthermore, the current density is an input variable. Based on the values of the operating conditions, the model predicts the molar fluxes and gas temperatures at the stack outlets, the average temperature of the solid material, the stack voltage and the average concentration of liquid water in the stack. Fig. 1 shows the solution variables and operating conditions and illustrates that these parameters are accessible even in a fully integrated fuel cell system. For the stack temperature, four monitoring points are indicated from which the average temperature is calculated.

The derivation of the model equations is done in a bottom-up approach that can be split up into three steps. First, we consider one particular cell of the stack. Balance equations are set up for a representative elementary volume of the cell (REV_1) and for a representative elementary channel (REC) in the cell (REV_2). The model is reduced to one geometrical dimension, the direction along the channel length. Second, the time-dependent balance equations for the REVs are integrated along the channel length. For a complete description of one cell all gas channels are assumed to behave like the REC. Third, the stack is modeled as several coupled cell modules. The approach and the model geometry is illustrated in Figs. 1–3. The model assumptions are

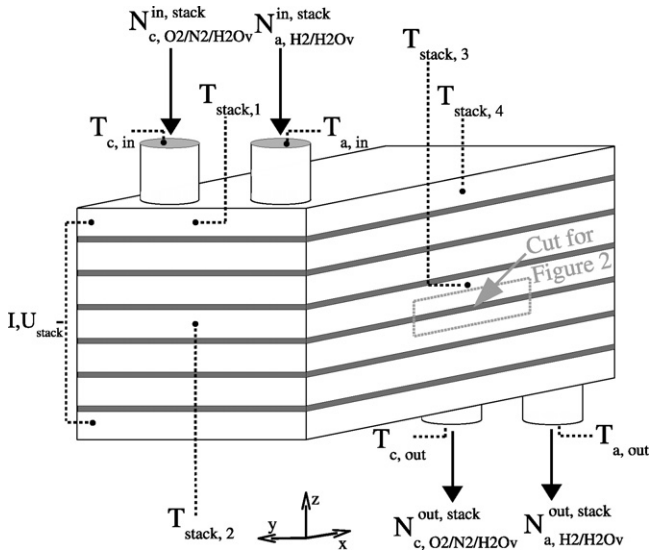

Fig. 1. 3D-View of a PEMFC stack consisting of six cells. The membrane–electrode assemblies between the bipolar plates are indicated in dark gray. The measurement points that were used for the characterization of the stack with respect to thermal and mass balance are indicated. The values obtained at these measurement points correspond to the input and solution variables of the model. The cut for Fig. 2 is indicated in light gray.

motivated by the preservation of computational efficiency which is required for the simulation of realistic load cycles in system simulation and for the application in NMPC. In contrast, more detailed model approaches, e.g. Refs. [26,27] require massive computational effort either in terms of memory usage or computing time or both. The validity of our approach is shown by a comparison of simulation and experimental results for different realistic load profiles.

2.2. Model assumptions

The model assumptions are listed below. The axis system is illustrated in Fig. 2.

- The gas channels are treated as plug-flow reactors. This approach is used by several other authors, e.g. Refs. [6,10,12,28–30] and is generally accepted. A good overview of approaches used for the modeling of gas flow in the channels is given in Refs. [3,4]. A uniform velocity profile and a complete and instantaneous mixing perpendicular to the direction of the gas flow is assumed. Thus, the gas velocity and concentrations within a gas channel are uniform in the y- and z-direction. The underlying assumption of laminar flow is widely used in fuel cell modeling, e.g. Refs. [16,21,31–33], and was also satisfied by a Reynolds number calculation.
- The stack temperature is constant in the y- and z-direction.
- Liquid water is assumed to exist in the form of small droplets on the surface of the gas channels [5]. As heat exchange with the solid material is much faster than with the gas, liquid water is further assumed to have stack temperature.
- The volume of the liquid water is assumed negligible. Hence, it has no influence on the gas transport in the channels.
- Cross-over of nitrogen, hydrogen and oxygen through the membrane is neglected.
- The electrochemical reactions and the transport processes are assumed to be homogeneous throughout the stack.
- The mass transport resistance of the gas diffusion layer is neglected.
- The electrical and thermal contact resistances are neglected.

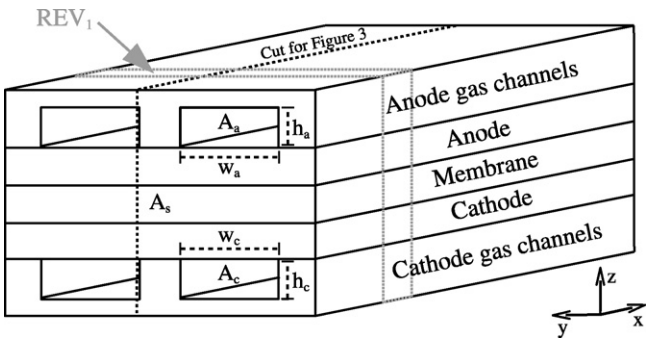

Fig. 2. 3D-View of the cell model corresponding to the cut in Fig. 1, indicating the cross-sectional area of the cell A_s and of the gas channels A_a and A_c, the representative elementary volume REV_1 as well as the cut for Fig. 3.

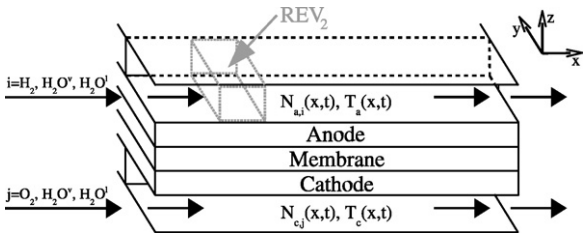

Fig. 3. Sideview of a cell along the cut indicated in Fig. 2, illustrating the direction of the molar flow $N_{a,i}$ of species i in the anode gas channel and the molar flow $N_{c,j}$ of species j in the cathode gas channel from the channel inlets to the channel outlets. The representative elementary volume REV_2 is exemplified for the anode gas channel.

Computational efficiency is mainly achieved by the following model characteristics: in order to reduce the number of modules to be calculated only one cell is modeled. The results are upscaled according to the number of cells in the stack. As an adequate modeling of the highly complex phenomena in the GDL and the membrane would require massive computational effort, the GDL is neglected and the membrane is assumed to be at steady-state. The spatially resolved characteristics of the fuel cell stack are neglected through the reduction of the model equations to ordinary differential equations in time.

3. Mathematical model

In the first step of the model derivation equations for energy and mass balance are formulated for a representative elementary volume of the solid material (REV_1) and of a representative gas channel (REV_2). As illustrated in Figs. 2 and 3, REV_1 corresponds to a section of a representative cell, whereas REV_2 is a channel section of a representative elementary gas channel. Mass balance equations are set up for hydrogen H_2, oxygen O_2, nitrogen N_2, water vapor H_2O^v, and liquid water H_2O^l in REV_2. The structure of the mass balance equations is identical for all

species:

$$\partial_t c_{k,i} = -(\nabla \cdot M_{k,i}) + R_{k,i}, \quad (1)$$

where the change in concentration $c_{k,i}$ of species i in volume element k is given by the divergence of the molar flow rate $M_{k,i}$ and by appropriate rates of production and consumption $R_{k,i}$. Energy balance equations are formulated for the gas channels of anode and cathode as well as for the solid material. Their basic structure is

$$\partial_t U_k = -(\nabla \cdot U_k v_{k,i}) - \nabla \cdot (\kappa \nabla T) + S_k, \quad (2)$$

where the change of internal energy U_k in volume element k is given by convective transport of energy associated with the mass average velocity $v_{k,i}$, transfer by heat conduction with the heat conduction coefficient κ, and energy production or consumption with the rate S_k.

As mentioned previously, we assume plug-flow conditions for the gas channels. Hence, Eq. (1) can easily be reduced to the following equation:

$$\partial_t c_{k,i}(x,t) A_k = -\partial_x N_{k,i}(x,t) + R_{k,i}(x,t) A_k, \quad (3)$$

where A_k is the cross-sectional area of REV_2 and $N_{k,i}$ is the molar flux of species i along the REV. Analogously, Eq. (2) for the energy balance of both REVs is reduced to

$$\partial_t U_k(x,t) = -\partial_x (U_k(x,t) v_{k,i}(x,t)) - \kappa \partial_x^2 T(x,t) + S_k(x,t). \quad (4)$$

As a consequence of this reduction, the mathematical model contains several effective parameters that include spatially distributed effects in the y–z-plane. In Section 6 it is described how these parameters are obtained. Below, the different balance equations are presented in the concise form corresponding to Eqs. (3) and (4), which is the form after step one of the derivation. Steps two and three are illustrated in Section 4. The parameters and symbols used in the model equations are listed in Tables 1 and 2. Table 3 contains a list of subscripts and superscripts.

3.1. Energy balance

3.1.1. Energy balance, gas channels

The following continuity equation describes the energy balance of the gaseous species in REV_2. The considered species are $i = H_2, H_2O^v$ for the anode and $i = O_2, N_2, H_2O^v$ for the cathode. Liquid water is assumed to exist in form of small droplets at the surface of the channels. The liquid water is assumed to be

Table 1
List of parameters and constants

Symbol	Explanation	Value	Reference
A_a	Cross-sectional area of anode gas channel	$(9 \pm 2) \times 10^{-7}\,m^2$	Meas.
$A_{a,sg}$	Heat exchange area per unit length between solid and gas, anode side	$(4.2 \pm 0.4) \times 10^{-3}\,m$	Meas.
A_c	Cross-sectional area of cathode gas channel	$(12 \pm 2) \times 10^{-7}\,m^2$	Meas.
$A_{c,sg}$	Heat exchange area per unit length between solid and gas, cathode side	$(4.6 \pm 0.4) \times 10^{-3}\,m$	Meas.
A_s	Cross-sectional area of cell	$(5.7 \pm 0.9) \times 10^{-5}\,m^2$	Meas.
A_{ss}	Heat exchange area between solid and surroundings per unit length	$(1.9 \pm 0.2) \times 10^{-2}\,m$	Meas.
C_{H_2}	Heat capacity of H_2	$28.8\,J\,mol^{-1}\,K^{-1}$	[37]
$C_{H_2O^l}$	Heat capacity of H_2O^l	$75.3\,J\,mol^{-1}\,K^{-1}$	[37]
$C_{H_2O^v}$	Heat capacity of H_2O^v	$33.6\,J\,mol^{-1}\,K^{-1}$	[37]
C_{N_2}	Heat capacity of N_2	$29.1\,J\,mol^{-1}\,K^{-1}$	[37]
C_{O_2}	Heat capacity of O_2	$29.3\,J\,mol^{-1}\,K^{-1}$	[37]
C_s	Specific heat capacity of stack solid material	$(770 \pm 40)\,J\,kg^{-1}\,K^{-1}$	Meas.
D^{ref}_{m,H_2O}	Diffusion coefficient of water in membrane for standard conditions	$5.5 \times 10^{-11}\,m^2\,s^{-1}$	[36]
d_y	Scaling factor for the channel width	2.2 ± 0.2	Meas.
F	Faraday constant	$96,485\,C\,mol^{-1}$	[38]
h_a	Height of anode gas channel	$(6 \pm 1) \times 10^{-4}\,m$	Meas.
h_c	Height of cathode gas channel	$(8 \pm 1) \times 10^{-4}\,m$	Meas.
ΔH_{vap}	Enthalpy of phase transition of water	$44,000\,J\,mol^{-1}$	[37]
k_{phase}	Condensation rate constant	$100\,s^{-1}$	[36]
$k_{m,p}$	Permeability of water in membrane	$1.58 \times 10^{-18}\,m^2$	[36]
L_{eff}	Effective channel length	$(465 \pm 2) \times 10^{-3}\,m$	Meas.
n_{cells}	Number of cells	6	Meas.
n_{chan}	Number of channels in each flow field	2	Meas.
R	Ideal gas constant	$8.314\,J\,K^{-1}\,mol^{-1}$	[38]
ΔS_a	Molar entropy of reaction at anode	$0.104\,J\,K^{-1}\,mol^{-1}$	[39]
ΔS_c	Molar entropy of reaction at cathode	$-326.36\,J\,K^{-1}\,mol^{-1}$	[39]
T^0	Reference temperature	298 K	Meas.
t_m	Thickness of membrane	$(250 \pm 1) \times 10^{-7}\,m$	Meas.
U^0_{oc}	Open-circuit voltage for standard conditions	1.23 V	Meas.
U_{sg}	Heat transfer coefficient between solid material and gas	$25\,W\,m^{-2}\,K^{-1}$	[5]
U_{ss}	Heat transfer coefficient between solid material and surroundings	$4.7 \pm 0.9\,W\,m^{-2}\,K^{-1}$	Meas.
w_q	Width of gas channel	$(1.5 \pm 0.1) \times 10^{-3}\,m$	Meas.
$\mu_{H_2O^l}$	Viscosity of H_2O^l	$3.56 \times 10^{-4}\,Pa\,s$	[37]
ρ_s	Average density of stack material	$2500 \pm 100\,kg\,m^{-3}$	Meas.

Table 2
List of symbols

Symbol	Explanation	Unit
A_k	Cross-sectional area of REV_2	m^2
A_q	Cross-sectional area of gas channel in electrode q	m^2
$a_{H_2O^v}$	Activity of water vapor	–
c_k	Constant with index k	–
$c_{k,i}$	Concentration of species i in volume element k	$mol\,m^{-3}$
$c_{q,i}$	Concentration of species i in gas channel q	$mol\,m^{-3}$
D_{m,H_2O}	Diffusion coefficient of H_2O in the membrane	$m^2\,s^{-1}$
I	Current	A
j	Current density	$A\,m^{-2}$
$j_{0,c}$	Cathodic exchange current density	$A\,m^{-2}$
$M_{k,i}$	Molar flow rate of species i in volume element k	$mol\,s^{-1}\,m^{-2}$
$N_{q,i}$	Molar flow of species i in gas channel q	$mol\,s^{-1}$
$N_{k,i}$	Molar flow of species i in REV_2	$mol\,s^{-1}$
$N_{q,i}^{in/out,rec}$	Molar flow of species i into/out of the REC of electrode q	$mol\,s^{-1}$
$N_{q,i}^{in,cell}$	Molar flow of species i into the gas inlet of the cell on the q side	$mol\,s^{-1}$
$N_{q,i}^{out,cell}$	Molar flow of species i out of the gas outlet of the cell on the q side	$mol\,s^{-1}$
$N_{q,i}^{in,stack}$	Molar flow of species i into the gas inlet of the stack on the q side	$mol\,s^{-1}$
$N_{q,i}^{out,stack}$	Molar flow of species i out of the gas outlet of the stack on the q side	$mol\,s^{-1}$
$N_{q,phase}$	Rate of phase change in electrode q	$mol\,s^{-1}\,m^{-1}$
n_{drag}	Electro-osmotic drag coefficient	–
P_q	Average pressure in gas channel q	Pa
$P_{q,sat}$	Saturation pressure in gas channel q	Pa
$p_{q,i}$	Partial pressure of species i in electrode q	Pa
p_i^0	Partial pressure of species i at reference conditions	Pa
$R_{k,i}$	Rate of consumption or production of species i in volume element k	$mol\,m^{-3}\,s^{-1}$
S_k	Rate of energy conversion in volume element k	$W\,m^{-3}$
T	Temperature	K
$T_{a,in}$	Gas temperature at anode gas inlet	K
$T_{a,out}$	Gas temperature at anode gas outlet	K
$T_{c,in}$	Gas temperature at cathode gas inlet	K
$T_{c,out}$	Gas temperature at cathode gas outlet	K
$T_{q,in/out}^{rec}$	Gas temperature at gas outlet/inlet of REC	K
T_q	Gas temperature in gas channel q	K
T_s	Stack temperature	K
$T_{s,av}$	Average stack temperature	K
T_{sur}	Temperature of surroundings	K
t	Time	s
U_{cell}	Cell voltage	V
$U_{k,i}$	Internal energy of species i in volume element k	$J\,m^{-3}$
U_{oc}	Open-circuit voltage	V
U_{stack}	Stack voltage	V
$v_{k,i}$	Velocity of species i in volume element k	$m\,s^{-1}$
$v_{q,i}$	Velocity of species i in gas channel q	$m\,s^{-1}$
z	Number of electrons exchanged in reaction	–
α	Symmetry factor	–
α_{net}	Net water migration coefficient	–
η_D^c	Activation losses in cathodic reaction	V
η_{oc}	Losses in open-circuit voltage	V
η_{ohm}	Ohmic losses	V
κ_s	Heat conduction coefficient of solid material	$W\,m^{-1}\,K^{-1}$
λ_m	Membrane water content	–
ν_i	Stoichiometry factor of species i	–
σ_m	Membrane conductivity	$S\,m^{-1}$

Table 3
Subscripts and superscripts

Symbol	Explanation
0	Reference conditions
a	Anode side
act	Active area
av	Average
c	Cathode side
cell	One cell in the stack
chan	Channel
drag	Electro-osmotic drag
eff	Effective
H_2O^l	Liquid water
H_2O^v	Water vapor
i	Species index
in	Gas inlet
j	Species index
k	Volume element
l	Liquid phase
m	Membrane
oc	Open-circuit
out	Gas outlet
phase	Phase transition
q	Anode or cathode
rec	Representative elementary channel
ref	Reference
s, stack	Of the stack
sg	Exchange between solid and gas
ss	Exchange between solid and surroundings
sur	Surroundings
v	Vapor phase

at stack temperature. The energy balance of the gas reads

$$\sum_i \partial_t [c_{q,i}(x,t) C_i T_q(x,t) A_q] = -\sum_i \partial_x [N_{q,i}(x,t) C_i T_q(x,t)] + A_{q,sg} U_{sg} [T_s(x,t) - T_q(x,t)] - \Delta H_{vap} N_{q,phase}(x,t), \quad (5)$$

where $q = a, c$ denotes the anode and the cathode side, respectively. i is the species index, $c_{q,i}$ is the concentration of species i in the channel q, C_i is the heat capacity, T_q is the gas temperature and A_q is the cross-sectional area of the REC, which equals A_k. $N_{q,i}$ is the molar flux of species i along the channel q. $A_{q,sg}$ is the heat exchange area between gas and solid material, U_{sg} is the corresponding heat exchange coefficient, T_s is the stack temperature. ΔH_{vap} is the enthalpy of evaporation and $N_{q,phase}$ is the rate of the phase change per unit length. The term on the left-hand side of the equation describes the change of internal energy in a volume element of unit length. The terms on the right-hand side describe from left to right: the transfer of internal energy by convection; the heat transfer between gas and solid stack material and the heat consumption or production due to evaporation and condensation of water.

3.1.2. Energy balance, solid material

The energy balance for the solid material in REV_1 links the processes in the gas channels of the anode and cathode.

It reads

$$\begin{aligned}
&\rho_s C_s A_s \partial_t T_s(x,t) \\
&= +n_{chan}\Delta H_{vap}[N_{a,phase}(x,t)+N_{c,phase}(x,t)] \\
&-n_{chan}d_y w_q\left[\left(\frac{\Delta S_a}{2F}+\frac{\Delta S_c}{4F}\right)T_s(x,t)-\eta_{oc}-|\eta_D^c|-\eta_{ohm}\right]j(x,t) \\
&-n_{chan}U_{sg}[A_{a,\,sg}(T_s(x,t)-T_a(x,t))+A_{c,\,sg}(T_s(x,t) \\
&-T_c(x,t))]+A_{ss}U_{ss}[T_{sur}(x)-T_s(x,t)]+A_s\kappa_s\partial_x^2 T_s(x,t) \\
&-n_{chan}\partial_x([N_{a,H_2O^l}(x,t)+N_{c,H_2O^l}(x,t)]C_{H_2O^l}T_s(x,t)),
\end{aligned} \tag{6}$$

where ρ_s is the density of the solid material, C_s is its heat capacity, A_s is the cross-sectional area of the cell and n_{chan} is the number of channels in each flow-field. d_y is a scaling coefficient, which takes into account the enlargement of the contact area between gas and membrane due to diffusion under land areas of the flow-field. w_q is the channel width, ΔS_q is the entropy of reaction in electrode q and F is the Faraday constant. The open-circuit losses are η_{oc}, the activation losses in the cathode are η_D^c and the ohmic losses are η_{ohm}. j denotes the current density, A_{ss} is the heat exchange area between stack and surroundings, U_{ss} is the heat transfer coefficient, T_{sur} denotes the temperature of the surroundings and κ_s is the heat conduction coefficient. The change of internal energy in the solid stack material in REV_1, which is described by the term on the left-hand side, is given by the following source and sink terms on the right-hand side of the equation: (a) heat generation and consumption due to condensation or evaporation of water in anode or cathode; (b) heat generation due to activation energy and irreversible losses; (c) heat transfer between bulk material and gases of anode and cathode side; (d) heat transfer between solid material and surroundings; (e) heat conduction driven by a temperature gradient within the stack; (f) heat transferred by convection of liquid water. As a cell contains several channels the terms (a)–(c) and (f) need to be multiplied with the number of channels n_{chan}.

3.2. Mass balance

For the mass balances of REV_2 the mass transport along the channel by convection, the fuel consumption of H_2 and O_2, the production of H_2O^v in the cathode side reaction, the evaporation and condensation of water as well as the transport of water vapor through the membrane are taken into account. Below only the mass balance equations for the species on the cathode side are given. The corresponding equations for the anode follow by analogy. The mass balance equation of oxygen in REV_2 on the cathode side is

$$\partial_t[c_{c,O_2}(x,t)A_c] = -\partial_x[N_{c,O_2}(x,t)] - \frac{d_y w_q I(x,t)}{4F}, \tag{7}$$

where c_{c,O_2} is the concentration and N_{c,O_2} is the molar flow of oxygen in REV_2. The concentration of oxygen changes due to convective transport along the channel and due to consumption of oxygen in the electrochemical reaction. The mass balance equation of water vapor in REV_2 on the cathode side reads

$$\begin{aligned}
\partial_t[c_{c,H_2O^v}(x,t)A_c] &= -\partial_x[N_{c,H_2O^v}(x,t)] - N_{c,phase}(x,t) \\
&+\frac{d_y w_q j(x,t)}{2F} + \frac{d_y w_q \alpha_{net} j(x,t)}{F},
\end{aligned} \tag{8}$$

where c_{c,H_2O^v} is the concentration and N_{c,H_2O^v} is the molar flow of water vapor in REV_2. The net water migration coefficient α_{net} describes the net-number of water molecules carried through the membrane per proton (Eq. (15)). The change in concentration of water vapor is balanced by: the convective transport of water vapor; the condensation or evaporation of water; the generation of water in the electrochemical reaction and the transport of water through the membrane. The mass balance equation for liquid water in REV_2 on the cathode side is

$$\partial_t[c_{c,H_2O^l}(x,t)A_c] = -\partial_x[N_{c,H_2O^l}(x,t)] + N_{c,phase}(x,t), \tag{9}$$

where c_{c,H_2O^l} is the concentration and N_{c,H_2O^l} is the molar flow of liquid water. The concentration of liquid water changes due to convective transport of liquid water along the channel and condensation or evaporation of water. The amount of water that condenses or evaporates in a volume element is modeled according to Golbert and Lewin [12]:

$$N_{c,phase}(x,t) = \frac{k_{phase} w_q h_c}{RT_c(x,t)}(p_{c,H_2O^v}(x,t) - P_{c,sat}(T_c(x,t))), \tag{10}$$

where k_{phase} is the condensation rate constant, h_c is the channel height, R is the ideal gas constant, p_{c,H_2O^v} denotes the partial pressure of water vapor in the cathode gas channel and $P_{c,sat}$ is the saturation pressure of water vapor, respectively. It is assumed that water condenses when $p_{c,H_2O^v} > P_{c,sat}$ and that existing liquid water evaporates when $p_{c,H_2O^v} < P_{c,sat}$.

3.3. Electrical model

The cell potential U_{cell} is calculated from the following equation [12]:

$$\begin{aligned}
U_{cell} &= U_{oc} - \eta_{oc} - |\eta_D^c| - \eta_{ohm} \\
&= U_{oc} - \eta_{oc} - \frac{RT_s}{\alpha z F}\ln\left(\frac{j(t)}{j_{0,c}}\right) - \frac{j(t)t_m}{\sigma_m(x,T,\lambda_m(t))},
\end{aligned} \tag{11}$$

where U_{oc} denotes the open-circuit voltage, which is calculated by the Nernst-equation given in Appendix A. α is the symmetry factor and z is the number of electrons exchanged in the reaction. $j_{0,c}$ is the cathodic exchange current density, t_m is the thickness of the membrane and σ_m is the membrane conductivity. The membrane conductivity σ_m depends on the membrane water content λ_m. To account for this, λ_m is calculated for each time-step. σ_m is calculated according to Springer et al. [34]:

$$\sigma_m = (0.00514\lambda_m - 0.00326)\exp\left(1268\left(\frac{1}{303}-\frac{1}{T_s}\right)\right). \tag{12}$$

3.4. Membrane model

The membrane water content λ_m is defined as

$$\lambda_m = \frac{n_{m,H_2O}}{n_{m,SO_3}}, \tag{13}$$

where n_{m,H_2O} is the number of water molecules and n_{m,SO_3} is the number of SO_3-groups in the membrane. The dependency of λ_m on the water vapor activity $a_{H_2O^v}$ is modeled according to [34]:

$$\lambda_m = \begin{cases} (0.043+17.8a_{H_2O^v}-39.85a^2_{H_2O^v}+36a^3_{H_2O^v}) & \text{for } a_{H_2O^v}\leq 1 \\ (14+1.4(a_{H_2O^v}-1)) & \text{for } a_{H_2O^v}>1. \end{cases} \tag{14}$$

The net water migration coefficient is given by [34]:

$$\alpha_{net} = n_{drag} - \frac{F}{j} D_{m,H_2O} \frac{c_{c,H_2O^v} - c_{a,H_2O^v}}{t_m} - \frac{c_{c,H_2O^v} + c_{a,H_2O^v}}{2} \frac{k_{m,p} F}{\mu_{H_2O^l} j} \frac{p_{c,H_2O^v} - p_{a,H_2O^v}}{t_m}, \tag{15}$$

where n_{drag} is the electro-osmotic drag coefficient. D_{m,H_2O} is the diffusion coefficient of water in the membrane, $k_{m,p}$ is the permeability and $\mu_{H_2O^l}$ the viscosity of liquid water. Hence, the transport of water through the membrane is given by electro-osmotic drag and diffusion due to a concentration and pressure gradient across the membrane.

4. Discretization

The stack model presented here simulates the most important parameters for the operation of a PEMFC stack, which are illustrated in Fig. 1. To derive appropriate and rapidly computable equations, the system of partial differential equations for the REVs described in Section 3 is integrated along the effective channel length L_{eff}. This corresponds to the second step of the model derivation as described in Section 2. The model equations after step one of the model derivation are formulated along the channel, that is, in the x-direction. This corresponds to assuming straight channels. Thus, L_{eff} is the geometrical length of the channel measured along the channel, even in a serpentine flow-field. With the aid of the Gaussian law and the mean value theorem, ordinary differential equations (ODEs) in time were derived which are discretized to the inlet and outlet of the gas channels or the cell's solid material, respectively. In the following the approach is exemplified for Eqs. (5) and (7). Integration of Eq. (5) along the channel length yields

$$\begin{aligned} &\sum_i C_i A_q \partial_t \int_0^{L_{eff}} (c_{q,i}(x,t) T_q(x,t))\,dx \\ &= -\sum_i C_i \int_0^{L_{eff}} \partial_x (N_{q,i}(x,t) T_q(x,t))\,dx \\ &\quad + A_{q,sg} U_{sg} \int_0^{L_{eff}} (T_s(x,t) \\ &\quad - T_q(x,t))\,dx - \Delta H_{vap} \int_0^{L_{eff}} N_{q,phase}(x,t)\,dx. \end{aligned} \tag{16}$$

Integration under use of the mean value theorem leads to

$$\begin{aligned} &A_q L_{eff} \sum_i C_i d_t(\overline{c_{q,i}}\,\overline{T_q}) \\ &= -\sum_i C_i (N^{out,rec}_{q,i} T^{rec}_{q,out} - N^{in,rec}_{q,i} T^{rec}_{q,in}) + L_{eff} A_{q,sg} U_{sg} (\overline{T_s} - \overline{T_q}) \\ &\quad - L_{eff} \Delta H_{vap} \overline{N_{q,phase}}. \end{aligned} \tag{17}$$

Rearranging Eq. (17) results in

$$\begin{aligned} d_t \overline{T_q} = \left[\sum_i C_i \overline{c_{q,i}}\right]^{-1} \cdot \Bigg[&-\overline{T_q} \sum_i C_i \overline{c_{q,i}} \\ &- \frac{1}{A_q L_{eff}} \sum_i C_i (N^{out,rec}_{q,i} T^{rec}_{q,out} - N^{in,rec}_{q,i} T^{rec}_{q,in}) \\ &+ \frac{A_{q,sg} U_{sg}}{A_q} (\overline{T_s} - \overline{T_q}) + \frac{\Delta H_{vap}}{A_q} \overline{N_{q,phase}} \Bigg]. \end{aligned} \tag{18}$$

Integrating Eq. (7) along the channel length yields

$$\begin{aligned} A_c \int_0^{L_{eff}} \partial_t [c_{c,O_2}(x,t)]\,dx = &- \int_0^{L_{eff}} \partial_x [N_{c,O_2}(x,t)]\,dx \\ &- \frac{d_y w_q}{4F} \int_0^{L_{eff}} j(x,t)\,dx. \end{aligned} \tag{19}$$

Using the mean value theorem integration leads to

$$d_t \overline{c_{c,O_2}(t)} = \frac{1}{A_c L_{eff}} [N^{in,rec}_{c,O_2}(t) - N^{out,rec}_{c,O_2}(t)] - \frac{d_y w_q \overline{j(t)}}{A_c 4F}. \tag{20}$$

Thus, balance equations are derived for the REC which are reduced to net flows at the channel inlet and outlet. Under the assumption that all gas channels in a cell behave like the REC net flows at the cell inlet and outlet are calculated through multiplication of the channel net flows with the number of channels in each electrode. Integration of Eq. (6) directly yields a net energy balance equation for the solid material of one complete cell in the stack. Hence, a system of equations is derived, which describes a complete cell module.

In step three of the model derivation the stack is modeled as several coupled cell modules. To preserve computational efficiency we assume that each cell in the stack works identically and that the fuel is distributed equally among the cells. Fig. 4 gives an overview of the input and solution variables of the model and illustrates how the variables are adapted from cell to stack level.

5. Numerical solution method

The discretized model equations form a linear-implicit system of differential-algebraic-equations (DAEs), which can be written as

$$M(y,t)\dot{y} = f(y,t) \tag{21}$$

with a singular mass matrix $M(y,t)$. The system is of index 1, that is, one derivation is necessary to transform the DAE-system into a system of ODEs. Numerically solving a DAE-system is

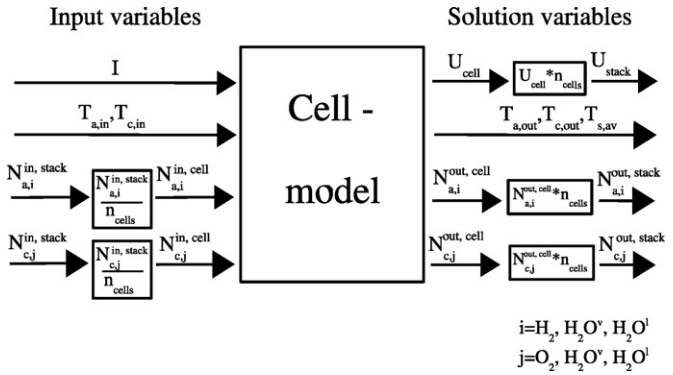

Fig. 4. Overview of the boundary conditions and the solution variables of the model. The conversion of the extensive variables from the stack scale to the cell scale is done by division through the number of cells n_{cells} or by multiplication with n_{cells}, respectively.

generally more complex than solving ODEs, as DAE-systems require consistent initial conditions. The model was implemented in MATLAB$^{\text{TM}}$ using the built-in solver ode15s of the ODE Solver environment which demonstrated good stability. Ode15s is a variable-order solver based on the numerical differentiation formulas capable of solving stiff DAE-systems of index 1 [40].

6. Parameter identification

The mathematical model described contains a high number of constants and parameters, which can be grouped into stack-dependent geometrical, electrochemical and physical parameters, as well as stack-independent physical constants. Finding suitable values for these parameters is one of the crucial points for the success of the model. The identification methods exemplified for the stack shown in Fig. 5 are easily transferable to different stack designs.

Most of the geometrical stack and flow-field parameters can be taken from direct measurements as illustrated in Fig. 2. However, due to the simplified model structure several geometrical parameters need to be adjusted accordingly. The stack used for model validation has a serpentine flow-field. As the model assumes straight channels the effective channel length L_{eff} corresponds to the geometrical channel length measured along the channel. The heat exchange area between solid and gas $A_{q,\text{sg}}$ equals the surface of one channel in flow-field q standardized to one unit length. The heat exchange area between solid and surroundings A_{ss} takes into account the surface of the cells, the endplates and the cooling fins. The surface area is divided by the number of cells and standardized to one unit length. The scaling coefficient d_y takes into account the enlargement of the contact area between gas and membrane due to diffusion under the land areas of the flow-field. For a well-designed flow-field it can be assumed that the whole active area is supplied with gases. Thus, d_y equals the ratio of active area and direct contact area between gas channels and GDL.

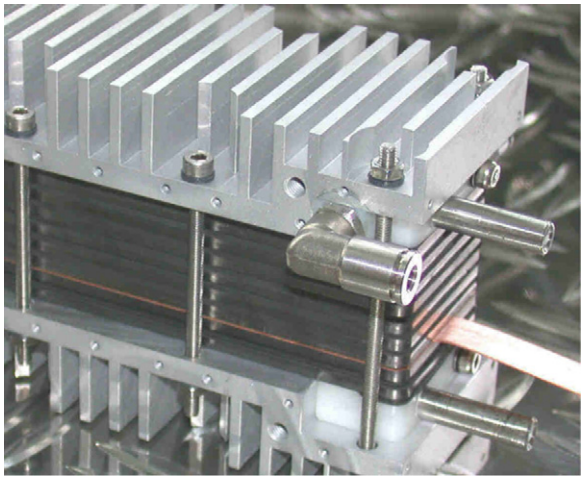

Fig. 5. Fuel cell stack used for parameter identification and model validation.

The physical and reaction parameters are determined by measurements and literature research as indicated in Table 1. The cathodic exchange current density $j_{0,\text{c}}$, the symmetry factor α and the losses in open-circuit voltage η_{oc} are identified through least-square-fits of Eq. (11) to IV-curves. The heat transfer coefficient between solid material and surroundings U_{ss} is identified on the basis of cooling curves monitoring the average stack temperature $T_{\text{s,av}}$ in a setting without gas and current flow. In this case the following equation can be deduced from Eq. (6):

$$\frac{\mathrm{d}T_{\text{s,av}}}{\mathrm{d}t} = \frac{U_{\text{ss}}A_{\text{ss}}}{\rho_{\text{s}}C_{s}A_{\text{s}}}(T_{\text{sur}}(t) - T_{\text{s,av}}(t)). \tag{22}$$

Integration leads to

$$T_{s,\text{av}}(t) = (T_{\text{s,av}}(t_0) - T_{\text{sur}}(t_0))\exp\left(-\frac{A_{\text{ss}}U_{\text{ss}}}{\rho_{\text{s}}C_{s}A_{\text{s}}}t\right) + \overline{T_{\text{sur}}}. \tag{23}$$

The parameter U_{ss} is determined through least-square-fits of Eq. (23) to measured cooling curves.

7. Experiment

In order to identify the dynamic behavior of a portable PEM fuel cell stack an experimental investigation was carried out. The portable stack used for the measurements was developed at the Fraunhofer ISE. It consists of six cells with an active cell area of 30.2 cm^2 each. A Gore Primea 5510 MEA with a platinum loading of 0.4 mg cm^{-2} is used. Cooling fins on the outer cells allow operation with passive cooling only. Due to its small geometrical dimensions the stack shows a pronounced dynamic behavior with respect to stack temperature and water management. Therefore, it is very well suited for a validation study of the dynamic stack model. In addition, the quick response of the stack to changes in the operating conditions allows short, controlled operation under critical conditions such as dry-out or flooding without damaging the stack. The particular stack is used for the implementation of NMPC in an ongoing project. Results of this work will be published elsewhere.

The measurements were carried out at a computer-controlled test stand, which controls the operating conditions of the stack as well as the data acquisition. Gas flow controllers manage the flow of hydrogen into the anode and oxygen or air into the cathode.

An external consumer is simulated by a galvanostat, which can subject the stack to arbitrary current profiles. The gas inlet flows as well as the voltages of each individual cell and of the whole stack are measured. The stack impedance is measured at 1 kHz. The stack temperature was measured with four thermocouples at the external surface of the stack as usually done in integrated fuel cell systems. As indicated in Fig. 1 the thermocouples were placed on the long and short sides of the top and of one of the middle cells in order to obtain a reasonable average value. It is assumed that due to the high thermal conductivity of the bipolar plates the temperature distribution throughout the stack balances quickly. This assumption is supported by the quick reaction of the measured stack temperature to changes in the load. In addition, a comparison of the measured temperatures of the four thermocouples showed a maximum deviation of only 2 K.

The stack was subjected to different load profiles, e.g. step and jump profiles during which it was supplied with pure hydrogen on the anode side and dry air on the cathode side. For each measurement the gas flow was kept at a constant rate, which corresponds to a stoichiometry of 2 for the highest current in the profile. The measurements were carried out under ambient pressure. The temperature of the surroundings was $T_{sur} = (298 \pm 1)$ K throughout the experiment. Each profile was measured several times to ensure reproducibility.

8. Results and discussion

For the validation study several profiles were simulated. Stable numerical convergence behavior was observed in all cases. The parameters used for the simulations are listed in Table 1. In the following, a step and a jump profile are discussed. For the step profile stack currents of $I = 1, 3, 6$ A were applied. The time-spans for each step were 3 min on the ascent and 6 min on the descent. For the later a longer interval was chosen to further investigate the cooling of the stack. The flow rates at the gas inlets were set to $0.7\,l\,\mathrm{min}^{-1}$ for hydrogen and $1.4\,l\,\mathrm{min}^{-1}$ for air. For the jump profile the current was alternated between 1 A and 5 A with a hydrogen flow rate of $0.6\,l\,\mathrm{min}^{-1}$ and an air flow rate of $1.2\,l\,\mathrm{min}^{-1}$. The simulations were carried out on an AMD Athlon 1533 MHz. Short computing times of 0.6 s for the step profile with a time of operation of 23 min and 0.8 s for the jump profile with a time of operation of 30 min are proofs of the numerical efficiency of the model.

8.1. Model validation

Validation of the model is performed by comparison of measured stack temperatures and voltages to the model predictions. Figs. 6 and 7 show a comparison between measured and simulated stack temperature for the step and the jump profile, respectively. The measured value is an average of the measurements of the four thermocouples. Simulation and experiment show good correlation. At high current the stack temperature increases due to the different loss mechanisms corresponding to term (b) in Eq. (6). Parametric studies showed that activation losses at the cathode are the dominant loss mechanism. The

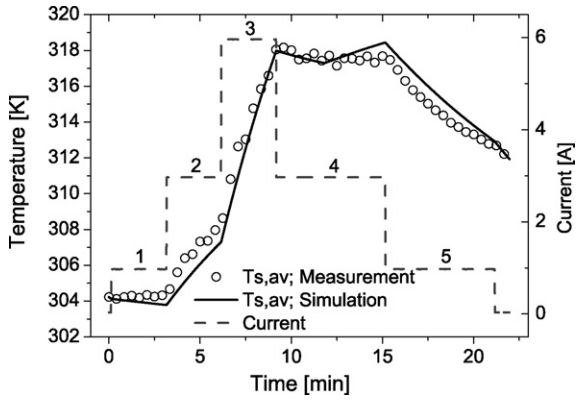

Fig. 6. Comparison between simulated and measured stack temperature for a current step profile. Simulation and experiment show good correlation. The break on step 4 is caused by the phase change enthalpy of water.

cooling of the stack is dominated by heat exchange between solid material and surroundings (term (d) in Eq. (6)), whereas only a small amount of heat is dissipated by the exhaust gases. It is noticeable that current changes affect the stack temperature almost without time-delay, even though the temperature was measured at the outside of the stack as indicated in Fig. 1. This is explained by the small thermal mass and the high heat conductivity of the solid stack material, hence validating the assumption of a homogeneous stack temperature in the y- and z-direction. Although the simulated and measured stack temperatures agree well, there are also slight deviations. It can be noted, that the deviations are mostly due to a slower increase and a faster decrease of the simulated stack temperature at low current (Fig. 6, steps 1 and 2; Fig. 7, steps with odd numbers), whereas at high current the slopes agree well. As the water production and therefore the degree of humidification of membrane and electrode is correlated with the current density, it can be concluded that a humidification-dependent heat source is not modeled comprehensively. This can be the heat dissipation due to insufficient humidification of the membrane–electrode assembly as well as inhomogeneous current distributions and losses throughout the stack. The break on step 4 in Fig. 6 is caused

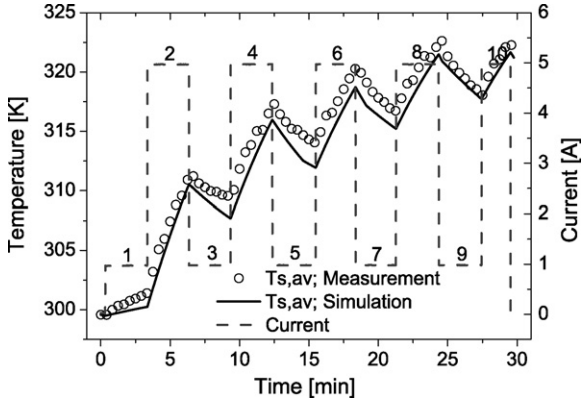

Fig. 7. Comparison between simulated and measured stack temperature for a current jump profile. Simulation and experiment agree well. Deviations can be explained by heat dissipation due to insufficient humidification of the electrode and inhomogeneous current density distribution.

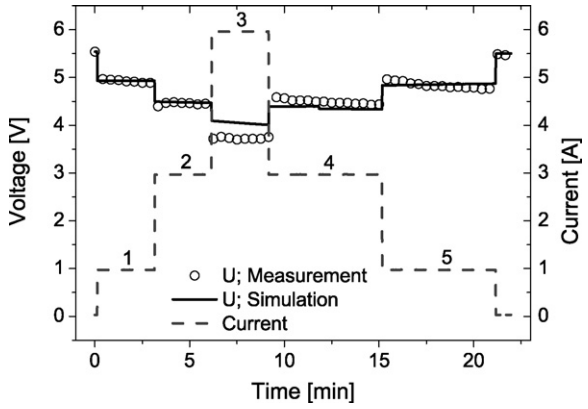

Fig. 8. Comparison between simulated and measured stack voltage for a current step profile. A good correlation is obtained. Deviations between model predictions and experiment are connected with critical operating conditions of the stack.

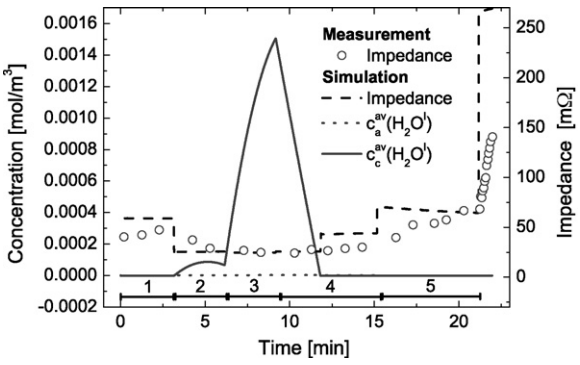

Fig. 10. Simulation results for the step profile indicate a high concentration of liquid water on the cathode side for steps 2–4. This coincides with low values of simulated and measured impedance on these steps. Observation of the average concentration of liquid water and the stack impedance can be used to predict critical operating conditions like flooding or dry-out.

by phase change enthalpy of water. In the simulation all liquid water has evaporated at this point as shown in Fig. 11. Heat consumption due to evaporation stops, which leads to an increase of the stack temperature. In the model this is reflected by a change of sign of term (a) in Eq. (6) ($N_{q,\text{phase}}$ is negative, when evaporation takes place and positive elsewise). In reality a remainder of water will longer exist in the GDL or the membrane leading to a milder change-over between the two regimes. A detailed discussion on water balance is given below. Similar breaks indicating the switch between the two regimes are visible on steps 5, 7 and 9 in Fig. 7. As the temperature level increases with the step number the amount of accumulated water throughout the preceding high current step gets smaller and evaporation gets faster. Therefore, the breaks on higher numbered steps occur closer to the preceding load change. As the stack was dry at the beginning of the profile no breaks occur on steps 1 and 3. The validity of this interpretation is shown after the discussion of water balance below. A comparison between measured and simulated stack voltage is shown in Figs. 8 and 9. Simulated and measured stack voltage agree well. Deviations between model predictions and experiment are connected with the water balance of the stack as discussed below and in Fig. 12. A satisfying

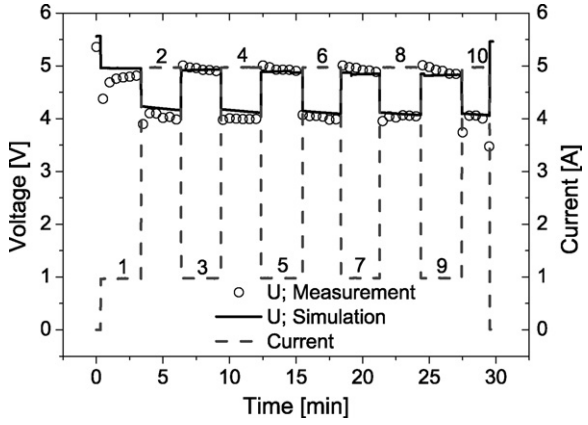

Fig. 9. Comparison between simulated and measured stack voltage for a current jump profile. Measurement and experiment agree well. The model parameters remain unchanged for each case of the validation study.

convergence behavior was also achieved for the other load profiles in the validation study. Thus, the model predictions for the stack temperature and the voltage are validated.

8.2. Water balance and critical operating conditions

Water management plays an important role for the operation of a PEMFC. Low concentrations of liquid water lead to a decrease in membrane conductivity whereas an accumulation of liquid water can block the gas flow due to flooding of electrode and gas channels. The stack model presented here incorporates mass balances of water vapor and liquid water (Eqs. (8) and (9)), which are linked through a phase change term (Eq. (10)). To allow prediction of critical operating conditions in an integrated fuel cell system, the stack model predicts the average concentrations of liquid water at the anode and cathode side and the impedance of the stack. Fig. 10 shows corresponding simulation results and experimental values of the stack impedance for the step profile. Simulation results indicate a high concentration of liquid water at the cathode side for steps 2–4. This coincides with low values of simulated and measured impedance on steps 2–4. As the membrane model is steady-state, the simulated values change rapidly upon a load change, whereas the experimental results indicate slower variations of membrane conductivity. However, the simulated impedance reflects the trend of the measurement well. In order to cover the dynamic behavior of the water impregnated into the membrane, a dynamic membrane model is necessary. Yet, models that describe the dynamic water transport through the membrane accurately are usually computationally expensive, see e.g. Ref. [35]. The development of a computationally efficient, dynamic membrane model is very challenging, but is seen as one of the key points to improve the predictive capability of dynamic PEMFC models. To illustrate the evolution of the average concentration of liquid water in the cathode, Fig. 11 shows the relation between phase transition of water, its partial pressure and the saturation pressure for the step profile. Water condenses when $p_{H_2O^v} > P_{c,\text{sat}}$ and liquid water evaporates when $p_{H_2O^v} < P_{c,\text{sat}}$ (Eq. (10)). It is assumed that the stack does not contain liquid water at the beginning of the

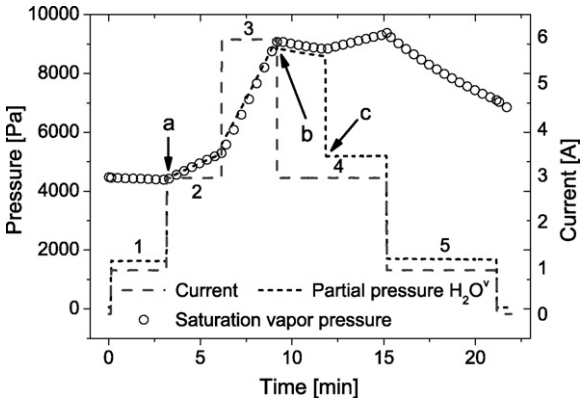

Fig. 11. Simulation results visualizing the relation between phase transition of water, its partial pressure $p_c(H_2O^v)$ and the saturation pressure $P_{c,sat}$ of water vapor on the cathode for the step profile. Condensation occurs between point a and b as $p_c(H_2O^v)$ is higher than $P_{c,sat}$. Liquid water evaporates between points b and c as $p_c(H_2O^v) < P_{c,sat}$ holds.

measurement. Condensation occurs during steps 2 and 3 starting at point (a), where $p_{H_2O^v}$ is higher than $P_{c,sat}$ due to the high production of water in the electrochemical reaction. This coincides with an increasing concentration of liquid water in these steps in Fig. 10. Condensation ends as $p_{H_2O^v}$ decreases due to lower water production after the load reduction (b). Existing liquid water evaporates in the course of several minutes (c). After this point due to the higher temperatures and the low load water exists in vapor form only and condensation or evaporation does not take place.

Predicting the impedance and the average concentration of liquid water, the model allows the early detection of critical operating conditions such as flooding or dry-out. However, the model does not yet predict the corresponding quantitative decrease in the stack voltage as the two-phase effects require detailed models on the micro-scale, which are not agreeable to the demand of limited computational effort. Fig. 12 illustrates the effects of the water balance on the stack voltage. The measured voltage curve shows three characteristics: humidification, flooding and dry-out. At step 2 the stack voltage increases as the membrane

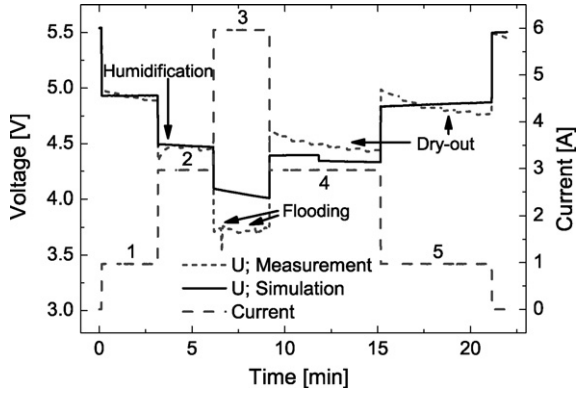

Fig. 12. Comparison of measured and simulated voltage for the current step profile indicating the effects of the water balance. The measured voltage curve shows three characteristics: humidification, flooding and dry-out. The simulated concentration of liquid water in Fig. 10 indicates the breakdown of the stack voltage due to flooding.

and electrode take up water. The opposite effect is observed during steps 4 and 5. The simulated average concentration of liquid water in Fig. 10 as well as the impedance indicate a low concentration of water in the stack. In step 3 the stack voltage shows flooding effects, which are not captured by the model. However, the simulated concentration of liquid water indicates the breakdown of the stack voltage due to flooding. Thus, observing the characteristics of the voltage allows a conclusion on the water balance of the stack. This also supports the validity of the interpretation of Fig. 7. During step 1 in Fig. 9 the voltage increases rapidly indicating a low, but increasing degree of membrane and electrode humidification, whereas throughout steps 3, 5, 7 and 9 the voltage decreases due to drying-out of the membrane. For higher numbered steps the decrease becomes much faster. Although the model does not capture the voltage decrease quantitatively, the position of the breaks in the simulated stack temperature in Fig. 7 shows that the regimes of high and low water concentration are modeled appropriately.

As Fig. 12 indicates the predictive capability of the model shows limitations when the stack is operated in a high current range. This is due to the negligence of the GDL and the simple model approach used for the membrane. Therefore, the highly complex two-phase effects in the membrane and the GDL are not covered. To develop a computationally efficient model, that includes the corresponding phenomena goes far beyond the scope of the present paper. In addition, the predictive capability of the model might show limitations for PEMFC stacks with a strong spatial inhomogeneity of temperature or electric potential. This is due to the fact that the gradients in temperature and electric potential across the stack need to be small to ensure the validity of the model approach.

9. Conclusions

In this work, a numerically efficient model was developed to study the dynamic response of a PEMFC stack subjected to load changes. The attribute of numerical efficiency was imposed in order for the model to be applicable for NMPC. Therefore, a reasonable compromise was found between computational effort and physical accuracy. Mainly three model properties make our calculations computationally efficient: firstly, only one cell is simulated and the results are then upscaled to account for the whole stack. Secondly, the spatial dependency of the fuel cell parameters is neglected as the energy and mass balance equations on which the model is based are reduced to ordinary differential equations in time. And thirdly, the GDL is not modeled and the membrane is assumed to be at steady-state as a detailed modeling of these cell parts would require massive computational effort. As a result of this approach the model proves to be computationally efficient: an operating time of 0.5 h can be simulated in less than 1 s. Despite the relatively simple model approach, the model and the calculation method could be validated against experimental data for different realistic load profiles through a comparison of measured and simulated stack voltage and stack temperature on time scales of up to 30 min. The model was used to study the run of the stack voltage and the stack temperature curves. Parametric studies showed that activa-

tion losses at the cathode cause the main mechanism of heating, whereas the heat exchange between solid and surroundings is the main mechanism for cooling. Slight deviations of the slope of the simulated stack temperature at low current indicate that a humidification-dependent heat source is not modeled comprehensively, which can be heat dissipation due to insufficient humidification of the membrane–electrode assembly as well as inhomogeneous current distributions throughout the stack. Furthermore, it is mentionable that current changes affect the stack temperature almost without time-delay, although the temperature was measured at the outside of the stack. This is explained by the small thermal mass and the high heat conductivity of the solid material.

In order to ensure reliable operation of a PEMFC under load changes it is essential to prevent critical operating conditions of flooding and dry-out, which depend on the highly complex phenomena of water balance of the stack. Therefore, we put special emphasis on the study of possibilities and limitations of the water balance description with respect to critical operating conditions within such a reduced model. Our model incorporates mass balance equations for water vapor and liquid water including a term for the phase change. For the purpose of studying the capability of this approach the stack was operated in critical states of flooding and dry-out. Through a comparison of measured and simulated stack voltage three characteristics of the stack voltage indicating humidification, flooding and dry-out of the stack are identified. Thereby indicating how the observation of the stack voltage allows a conclusion on the water balance of the stack. The model was successfully applied to predict the regimes of high and low water concentrations in the stack. It is shown, that by monitoring the simulated stack impedance and the average concentration of liquid water in the stack critical states of operation can be predicted. However, the model does not yet capture the corresponding quantitative change of the stack voltage as the underlying two-phase effects require detailed descriptions on the micro-scale which are not compatible with the demand for limited computing time.

With our model we have demonstrated that the dynamic response of a PEMFC stack under load changes can be simulated in short computing times with sufficient accuracy. Efforts are currently underway to implement NMPC algorithms based on this model. In order to further improve the predictive capabilities of the model future work could include the development of a computationally efficient, dynamic membrane model as well as the integration of a GDL model to improve simulation results when the stack is operated in a high current range.

Acknowledgements

The authors would like to thank J.O. Schumacher for his valuable contribution to the work presented here. Part of the author's research was funded by the German Federal Ministry of Education and Research (BMBF) via the project 'Model based design of fuel cells and fuel cell systems: PEM-Design (03SF0310A)'. Part of the work took also benefit from the project 'Optimal control of small fuel cells (MBZ6)' commissioned by the Landesstiftung Baden-Wuerttemberg foundation.

Appendix A

A.1. Supporting equations

The internal energy $U_{k,i}$ of species i in volume element k is given by

$$U_{k,i} = c_{k,i} C_i T_k. \tag{24}$$

The open-circuit voltage U_{oc} is calculated using the Nernst-equation:

$$U_{oc} = U_{oc}^0 + \frac{\Delta S_{mol}}{2F}(T - T^0) - \frac{RT}{2F}\sum_i \nu_i \ln\left(\frac{p_i}{p_i^0}\right), \tag{25}$$

where U_{oc}^0 is the open-circuit voltage at reference conditions, ΔS_{mol} is the molar entropy of the overall reaction and T^0 is the reference temperature. ν_i denotes the stoichiometry factor, p_i is the partial pressure and p_i^0 is the partial pressure of species i at reference conditions. The partial pressure p_i of the gas species i is calculated using Dalton's law:

$$p_i = \frac{N_{q,i}}{\sum_j N_{q,j}} P_q, \tag{26}$$

where P_q is the average pressure in gas channel q. Assuming that the gases in the channels can be treated as ideal, the following equation is used to calculate the concentration $c_{q,i}$ from the molar flow $N_{q,i}$:

$$c_{q,i} = \frac{N_{q,i}}{A_q v_{q,i}}, \tag{27}$$

where $v_{q,i}$ is the velocity of species i in electrode q.

The electro-osmotic drag coefficient n_{drag} is calculated according to Springer et al. [34]:

$$n_{drag} = (5/44)\lambda_m. \tag{28}$$

The following empirical equation is used to calculate the saturation pressure of water vapor [34]:

$$P_{q,sat} = c_{P1} x 10^{(c_{p2} + c_{p3}(T_q - 273) + c_{P4}(T_q - 273)^2 + c_{P5}(T_q - 273)^3)}. \tag{29}$$

with $c_{P1} = 101,325$, $c_{P2} = -2.18$, $c_{P3} = 2.95 \times 10^{-2}$, $c_{P4} = -9.18 \times 10^{-5}$ *and* $c_{P5} = 1.44 \times 10^{-7}$. The diffusion coefficient of water in the membrane D_{m,H_2O} as a function of λ_m and T_s was described by Golbert and Lewin [36] as

$$D_{m,H_2O} = n_{drag} D_{m,H_2O}^{ref} \exp\left(c_{D1}\left(\frac{1}{T_{\sigma,ref}} - \frac{1}{T_s}\right)\right) \tag{30}$$

with the empirical values $c_{D1} = 2416$ and $T_{\sigma,ref} = 303\,K$ [36]. D_{m,H_2O}^{ref} is the diffusion coefficient of water in the membrane at reference conditions.

The activity of water in channel q is calculated according to Golbert and Lewin [36]:

$$a_{H_2O^v} = \frac{N_{q,H_2O^v}}{\sum_i N_{q,i}} \frac{P_q}{P_{q,sat}}. \tag{31}$$

The reaction entropy of the overall reaction ΔS_{mol} for the consumption of 1 mol H_2 is calculated from the reaction entropy at the anode ΔS_a and the cathode ΔS_c:

$$\Delta S_{mol} = \Delta S_a + \frac{\Delta S_c}{2}. \quad (32)$$

References

[1] Q. Yan, H. Toghiani, H. Causey, J. Power Sources 161 (2006) 492–502.
[2] F. Allgöwer, T. Bodgwell, J. Qin, J. Rawlings, S. Wright, in: P. Frank (Ed.), Advances in Control, Highlights of ECC'99, Springer, London, 1999, pp. 391–449.
[3] K. Yao, K. Karan, K. McAuley, P. Oosthuizen, B. Peppley, T. Xie, Fuel Cells 4 (2004) 3–29.
[4] C.-Y. Wang, Chem. Rev. 104 (2004) 4727–4766.
[5] J. Yi, T. Nguyen, J. Electrochem. Soc. 145 (1998) 1149–1159.
[6] T. Fuller, J. Newman, J. Electrochem. Soc. 140 (1993) 1218–1225.
[7] T. Springer, M. Wilson, S. Gottesfeld, J. Electrochem. Soc 140 (1993) 3513–3526.
[8] J. Amphlett, R. Mann, B. Peppley, P. Roberge, A. Rodrigues, J. Power Sources 61 (1996) 183–188.
[9] J. Lee, T. Lalk, J. Power Sources 73 (1998) 229–241.
[10] M. Ceraolo, C. Miulli, A. Pozio, J. Power Sources 113 (2003) 131–144.
[11] Y. Shan, S.-Y. Choe, J. Power Sources 145 (2005) 30–39.
[12] J. Golbert, D. Lewin, J. Power Sources 135 (2004) 135–151.
[13] X. Yu, B. Zhou, A. Sobiesiak, J. Power Sources 147 (2005) 184–195.
[14] P. Pathapati, X. Xue, J. Tang, Renew. Energy 30 (2005) 1–22.
[15] D. McKay, W. Ott, A. Stefanopoulou, Proceedings of IMECE, 2005, pp. 1–10.
[16] S. Um, C.-Y. Wang, K. Chen, J. Electrochem. Soc. 147 (2000) 4485–4493.
[17] Y. Wang, C.-Y. Wang, Electrochim. Acta 50 (2005) 1307–1315.
[18] S. Shimpalee, W.-K. Lee, J. Van Zee, H. Naseri-Neshat, J. Power Sources 156 (2006) 355–368.
[19] S. Shimpalee, W.-K. Lee, J. Van Zee, H. Naseri-Neshat, J. Power Sources 156 (2006) 369–374.
[20] Y. Wang, C.-Y. Wang, Electrochim. Acta 51 (2006) 3924–3933.
[21] H. Guilin, F. Jianren, J. Power Sources 165 (2007) 171–184.
[22] C. Ziegler, H. Yu, J. Schumacher, J. Electrochem. Soc. 152 (2005) A1555–A1567.
[23] H. Wu, X. Li, P. Berg, Int. J. Hydrogen Energy 32 (2007) 2022–2031.
[24] A. Shah, G.-S. Kim, P. Sui, D. Harvey, J. Power Sources 163 (2007) 793–806.
[25] A. Shah, P. Sui, G.-S. Kim, S. Ye, J. Power Sources 166 (2007) 1–21.
[26] T. Berning, N. Djilali, J. Electrochem. Soc. 150 (2003) A1589–A1598.
[27] Y. Wang, C.-Y. Wang, J. Electrochem. Soc. 153 (2006) A1193–A1200.
[28] T. Nguyen, R. White, J. Electrochem. Soc. 140 (1993) 2178–2186.
[29] K. Dannenberg, P. Ekdunge, G. Lindbergh, J. Appl. Electrochem. 30 (2000) 1377–1387.
[30] S.-H. Ge, B.-L. Yi, J. Power Sources 124 (2003) 1–11.
[31] P. Nguyen, T. Berning, N. Djilali, J. Power Sources 130 (2004) 149–157.
[32] M. Hu, A. Gu, M. Wang, X. Zhu, L. Yu, Energy Convers. Manage. 45 (2004) 1861–1882.
[33] S. Maharudrayya, S. Jayanti, A. Deshpande, J. Power Sources 138 (2004) 1–13.
[34] T. Springer, T. Zawodzinski, S. Gottesfeld, J. Electrochem. Soc 138 (1991) 2334–2341.
[35] A. Weber, J. Newman, J. Electrochem. Soc. 151 (2004) A326–A339.
[36] J. Golbert, D. Lewin, J. Power Sources 135 (2004) 135–151.
[37] P. Atkins, Physical Chemistry, Oxford University Press, Oxford, 1994.
[38] R. Bird, W. Stewart, E. Lightfoot, Transport Phenomena, 2nd ed., Wiley, New York, 2001.
[39] M. Lampinen, M. Fomino, J. Electrochem. Soc. 140 (1993) 3537–3546.
[40] L.F. Shampine, M. Reichelt, J. Kierzenka, SIAM Review 41 (1999) 538–552.